Intergranular pitting corrosion of CoCrMo biomedical implant alloy

Pooja Panigrahi,[1] Yifeng Liao,[1] Mathew T. Mathew,[2] Alfons Fischer,[2] Markus A. Wimmer,[2] Joshua J. Jacobs,[2] Laurence D. Marks[1]

[1]Department of Materials Science and Engineering, Northwestern University, Evanston, Illinois
[2]Department of Orthopedic Surgery, Rush University Medical Center, Chicago, Illinois

Abstract: CoCrMo samples of varying microstructure and carbon content were electrochemically corroded *in vitro* and examined by scanning electron microscopy and electron backscatter diffraction techniques. The rate of corrosion was minimized (80% reduction from i_{corr} = 1396 nA/cm^2 to i_{corr} = 276 nA/cm^2) in high-carbon CoCrMo alloys which displayed a coarser grain structure and partially dissolved second phases, achieved by solution annealing at higher temperatures for longer periods of time. The mechanism of degradation was intergranular pitting corrosion, localized at phase boundaries and grain boundaries of high energy (high-angle and low lattice coincidence, $\Sigma 11$ or higher); grain boundaries of lower energy did not appear to corrode. This suggests the possibility of grain boundary engineering to improve the performance of metal implant devices. © 2013 Wiley Periodicals, Inc. J Biomed Mater Res Part B: Appl Biomater, 102B: 850–859, 2014.

Key Words: cobalt–chromium (alloy), hip prosthesis, microstructure, total joint replacement, corrosion

How to cite this article: Panigrahi P, Liao Y, Mathew MT, Fischer A, Wimmer MA, Jacobs JJ, Marks LD. 2014. Intergranular pitting corrosion of CoCrMo biomedical implant alloy. J Biomed Mater Res Part B 2014:102B:850–859.

INTRODUCTION

A variety of conditions, most notably osteoarthritis and rheumatoid arthritis, may result in a patient's need for prosthetic joint implants at hips and knees. Every year, as patients live longer and younger patients become candidates for joint replacement, the demand for hip replacements rises. Hip implants are becoming more common with the older population, with the number of total hip arthroplasties (THA) performed annually in the U.S. expected to grow 174% from 2005 to 572,000 by 2030.[1]

The CoCrMo alloy has been approved as an implantable biomedical material since the 1970s.[2] Advantages of using a metal for this application are mainly in the bulk mechanical properties, which can be predictably modified by various processing techniques such as casting, annealing, hot forging, and cold working.[3–7] Of the different articulating joint interfaces available for hip implants, metal-on-metal (MoM) is known to have one of the lowest wear rates, compared to systems with polyethylene.[2] However, recently the usage of MoM joints has diminished due to the serious clinical concerns that were reported associated with metal ions release to the surrounding tissues and host body.[8]

One of the major degradation processes that inevitably affect all metallic implants *in vivo* is corrosion.[9–11] While cobalt–chromium is especially corrosion resistant due to the passive film (Cr_2O_3) that forms in any oxidizing environment,[6] cobalt and chromium cations have been routinely detected in serum from patients with implants[12–15]; molybdenum forms water soluble ionic species that are presumed to readily leave the body. Complications observed clinically as a result of corroding CoCrMo at hip joints include hypersensitivity, metallosis (metallic staining of the surrounding tissue), excessive periprosthetic fibrosis, muscular necrosis, and vasculitis (patch inflammation of the wall of small blood vessels).[8] There are currently minimal ASTM/FDA regulations concerning the microstructure of CoCrMo joint implants, for instance there are no requirements concerning vol% of precipitates and exact temperatures for thermomechanical processing history. ASTM F1537 does call for a maximum grain size of 56.6 μm, but the effects of grain size within this range (sub-micron to grain size 5) are not detailed with any recommendations with respect to corrosion behavior.[16] This study analyzes how processing and microstructure have a direct effect on the corrosion resistance of this commonly used biomedical implant material and also delineates that the distribution of grain boundaries have an important, perhaps critical role with high-energy boundaries corroding substantially faster. We note that this suggests that classic metallurgical techniques can be used to minimize corrosion, although some important unknowns merit further study.

Correspondence to: L.D. Marks (e-mail: l-marks@northwestern.edu)

TABLE I. Exact Compositions of CoCrMo Wrought Alloy Specimens

Wt%	Co	Cr	Mo	C	Mn	Si	Ni	Fe
High-carbon	Balance	27.63	6.04	0.241	0.7	0.66	0.18	0.14
Low-carbon	Balance	27.56	5.7	0.034	0.6	0.38	0.55	0.19

MATERIALS AND METHODS

Samples

Both high-carbon (HC) and low-carbon (LC) samples were used in this study, with an emphasis on the former due to its higher current prevalence in the MoM industry.[2] Twenty cylindrical wrought CoCrMo alloy pins, 12 mm in diameter and 7 mm thick, were obtained from ATI Allvac, US. Fifteen pins were of high-carbon (HC) content and five pins were of low-carbon (LC) content in accordance with ASTM F 1537-08.[16] Exact compositions of the wrought alloy pins are given in Table I.

The HC and LC wrought alloy pins were annealed at solution heat treatment temperatures previously investigated by several authors[3,17–19] either for a short (2-h) or long (24-h) anneal time. The 10 experimental conditions are detailed in Table II, with the HC alloy samples heat-treated and corroded in triplicate ($n = 3$) to ensure statistical reliability of the data. All solution anneals were performed in an air furnace, and any surface oxides forming on the surface were mechanically removed using SiC grinding paper.

The solution-annealed CoCrMo alloy pins were polished to a mirror finish ($R_a \leq 10$ nm) using a mechanical polishing sequence of polycrystalline colloidal abrasive solutions on commercially available Texmet polishing cloths. The microstructure was analyzed following a chemical etch by a 2–5 min immersion in a solution of 50 mL H_2O and 50 mL HCl with 4 g of $K_2S_2O_5$ as a reagent.

Electrochemical corrosion testing

Samples were mechanically re-polished to remove any bulk surface impurities and etching artifacts immediately prior to electrochemical corrosion testing. Each sample was then incorporated into a custom made four-chamber electrochemical cell as the working electrode (WE) with a graphite counter electrode (CE) and saturated calomel electrode (SCE) reference electrode (RE), connected to a potentiostat monitored by an electrochemical analysis software supplied by Gamry Instruments. The corrosion cell was filled with 10 mL of bovine calf serum (BCS) with a protein content of 30 g/L) buffered to a basic pH 7.4 solution, and placed in a hot water bath maintained at 37°C to mimic physiological conditions.

TABLE II. Solution-Annealing Heat Treatments Performed on CoCrMo Wrought Alloy

Samples	Temperature (°C)	Time Annealed (h)
1 LC, 3 HC	–	–
1 LC, 3 HC	1150	2
1 LC, 3 HC	1150	24
1 LC, 3 HC	1230	2
1 LC, 3 HC	1230	24

A standard protocol was used to conduct the electrochemical tests. Each test began with a potentiostatic test, applying a constant cathodic potential (−0.9 V), which is an electrochemical cleaning process of the exposed area to remove the passive film and any contaminants that may have adsorbed on the metallic surface.[20] This ensured that all samples had similar surface conditions prior to data acquisition. An open circuit potential test (OCP initial) was run before any corrosion was performed to determine the material's open circuit potential (E_{oc}). Then, an electrochemical impedance spectroscopy (EIS) test was conducted. The EIS measurements were performed in the frequency range from 100 kHz to 10 mHz, with an AC sine wave amplitude of 10 mV applied at its open circuit potential. Results from this test were used to construct equivalent circuits (ECs) as a Randles circuit of a solution resistance R_u in series with a polarization resistance R_p and non-ideal capacitance (or constant phase element, CPE) C_f in parallel. The polarization resistance stems from the kinetics of the half cell reactions controlling the speed of the electrochemical reaction at the interface. When the working electrode (CoCrMo) is polarized above or below

TABLE III. Electrochemical Testing Sequence and Parameters

Test	Parameter	Value
OCP (initial)	Total time (s)	1800
	Stability (mV/s)	0
	Sample period (s)	0.1
Potentiostatic	Initial E (V) vs. E_{ref}	−0.9
	Initial time (s)	600
	Final E (V)	−0.9
	Final time (s)	0
	Sample period (s)	1
	Limit I (mA/cm^2)	25
	Open circuit E (V)	−0.232233
Electrochemical impedance spectroscopy	DC voltage (V) vs. E_{oc}	0
	AC voltage (mV ms)	10
	Initial frequency (Hz)	100000
	Final frequency (Hz)	0.005
	Points/decade	10
	Open circuit E (V)	−0.367033
Cyclic polarization (potentiodynamic)	Initial E (V) vs. E_{ref}	−0.8
	Apex E (V) vs. E_{ref}	1.8
	Final E (V) vs. E_{ref}	−0.8
	Forward scan (mV/s)	2
	Sample period (s)	0.5
	Reverse scan (mV/s)	2
	Apex I (mA/cm^2)	25
	Open circuit E (V)	−0.367033
OCP (after polarization)	Total time (s)	1800
	Stability (mV/s)	0
	Sample period (s)	0.1

TABLE IV. Electrochemical Results from Potentiodynamic Test and Electrochemical Impedance Spectroscopy

HC CoCrMo Samples	i_{corr} (nA/cm^2)	E_{corr} (V) vs SCE	E_{oc} Initial (V) vs SCE	E_{oc} After Polarization (V) vs SCE	Polarization Resistance, R_p (kΩ)	Capacitance, C (μF)
No HT	1396 ± 323	−0.747 ± 0.003	−0.481 ± 0.021	−0.407 ± 0.007	542 ± 190	20.54 ± 1.94
1150°C, 2 h	152.4 ± 60.3	−0.736 ± 0.002	−0.540 ± 0.073	−0.396 ± 0.007	491 ± 163	23.63 ± 5.23
1150°C, 24 h	281 ± 181	−0.745 ± 0.011	−0.412 ± 0.039	−0.409 ± 0.033	456 ± 87	17.33 ± 2.01
1230°C, 2 h	308 ± 198	−0.737 ± 0.015	−0.525 ± 0.096	−0.392 ± 0.009	408 ± 192	23.14 ± 6.81
1230°C, 24 h	276 ± 157	−0.752 ± 0.002	−0.428 ± 0.107	−0.328 ± 0.079	420 ± 234	17.94 ± 4.53

its open circuit potential, an electrical double layer with ions next to the working electrode forms, thus creating charges separated by an insulator, functioning as a capacitor. A CPE was used in place of an ideal capacitance in order to take into account the non-equilibrium current distribution due to surface roughness.

A potentiodynamic (cyclic polarization) test was performed to corrode the sample and measure the current at each applied potential. Preliminary studies were conducted to determine the ideal scan rate of the alloy in bovine calf serum. The samples were anodically polarized from −0.8 V to 1.8 V at a scan rate of 2 mV/s during the forward scan followed by a cathodic shift from 1.8 V back down to −0.8 V. A 2 mV/s scan rate was used to incorporate a faster experimental throughput while maintaining a sufficiently low scan rate to minimize the effects of uncharged capacitors at the double layer. The electrochemical parameters, corrosion potential (E_{corr}) and current density (i_{corr}) were estimated using Tafel's method.[21,22] Lastly, another open circuit potential test (OCP after polarization) was performed to measure the open circuit voltage E_{oc} of the corroded sample surface. Parameters of the electrochemical testing are provided in Table III.

Scanning electron microscopy

The microstructures of the annealed CoCrMo wrought alloys and the morphologies after corrosion were investigated by scanning electron microscopy using a Hitachi S-3400 SEM.
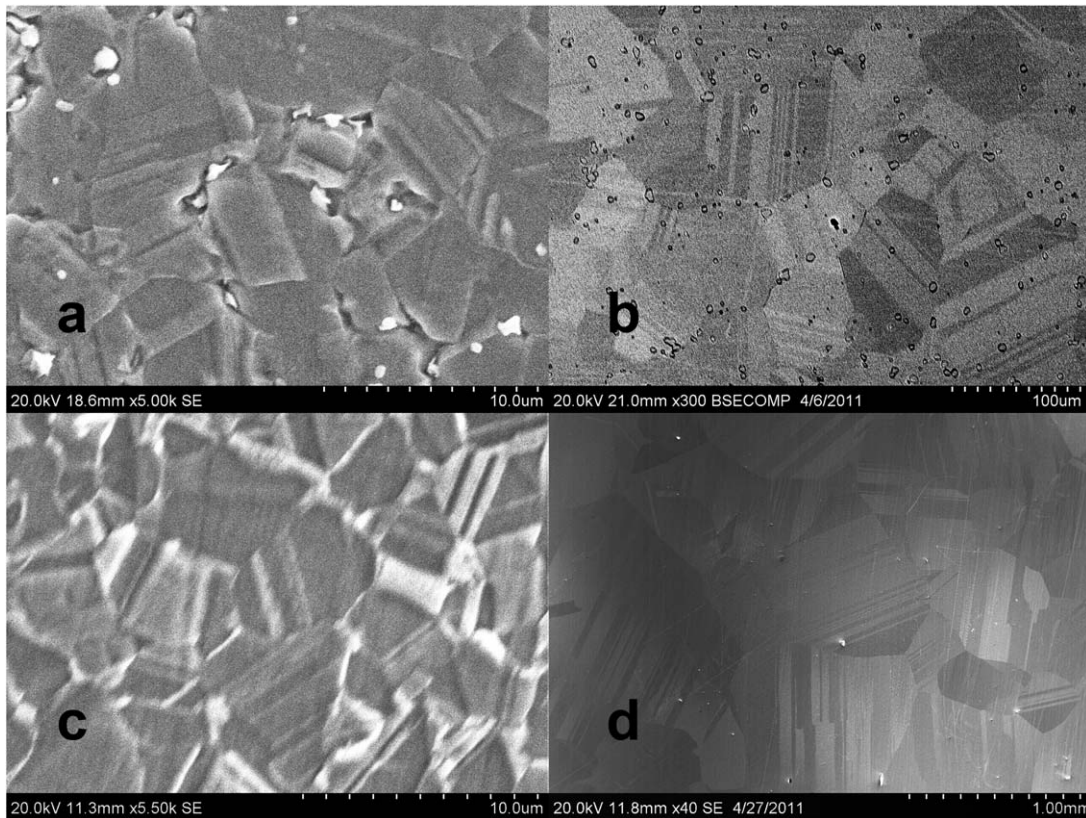

FIGURE 1. (a) Wrought HC CoCrMo alloy, as-received. Fcc-Co grains 3–5 μm in diameter with twinned microstructure. Carbide and intermetallic second phases observed mostly at grain boundaries; (b) solution-annealed (1150°C, 24 h) HC CoCrMo alloy. Fcc-Co grains 30–60 μm in diameter with twinned microstructure. Partially dissolved carbide and intermetallic second phases. Remaining second phases observed mostly at grain boundaries; (c) wrought LC CoCrMo alloy, as-received. Fcc-Co grains 3–5 μm in diameter with twinned microstructure. No observed carbide or intermetallic second phases; (d) solution-annealed (1230°C, 24 h) LC CoCrMo alloy. Fcc-Co grains 200–600 μm in diameter with twinned microstructure. No observed carbide or intermetallic second phases.
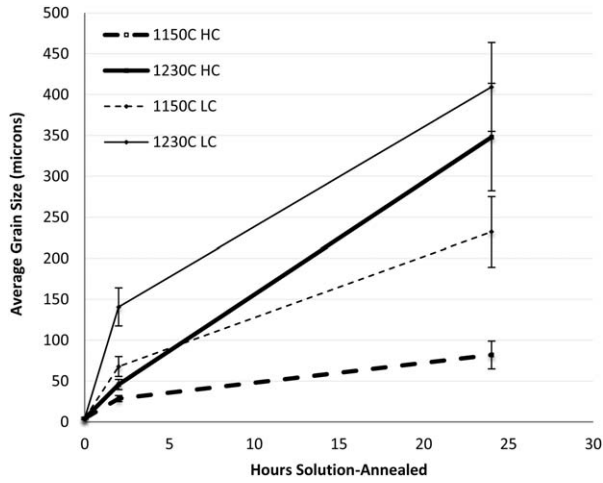
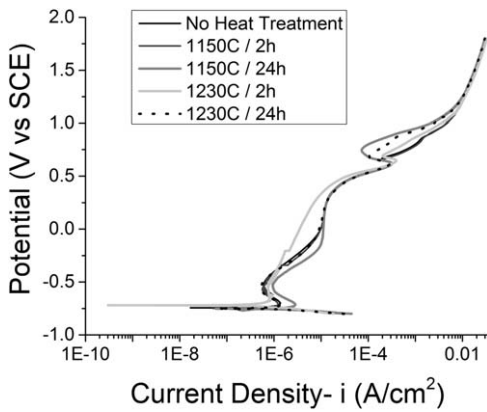**FIGURE 2.** Effects of solution-annealing on fcc-Co matrix average grain size.

FIGURE 3. Potentiodynamic curves of solution-annealed HC CoCrMo wrought alloys.

Secondary electron (SE) and backscattered electron (BSE) images were recorded at 20 kV and at a probe current of 70 μA. The presence of second phases, grain boundaries, and twin boundaries were observed for solution-annealed samples prior to corrosion, and the morphological topographic features were observed for samples after electrochemical testing.
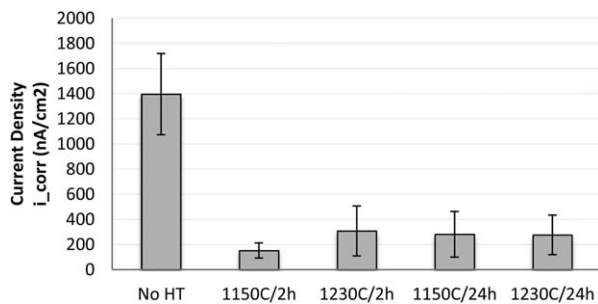

FIGURE 4. Current density i_{corr} at corrosion potential for solution-annealed HC CoCrMo wrought alloys.
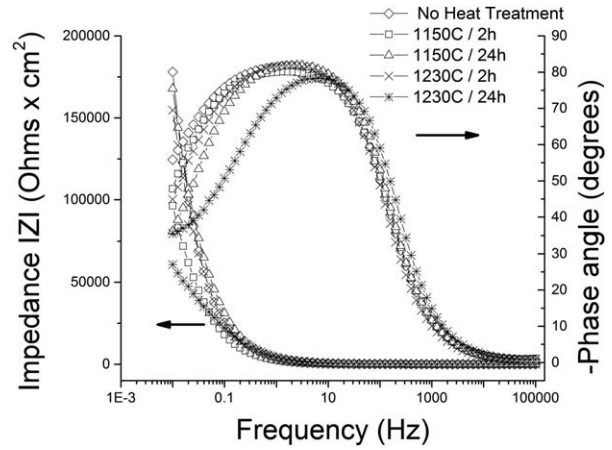

FIGURE 5. Experimental Bode plots of solution-annealed HC CoCrMo. A representative Bode impedance and phase curve was chosen for each solution-annealed condition; impedance data was obtained in triplicate.

White light interferometry

A Zygo white light interferometer with Mirau 20× objective lens was used to quantitatively measure topographic variation in the corroded surfaces and ensure a low enough roughness in the samples prior to corrosion testing ($R_a <$ 10 nm). The white light interferometer had a lateral resolution limited by the wavelength of light and a finer z-axis resolution limited only by the sensitivity of the light intensity detector,[23] and was used to measure the depth of more heavily corroded regions with respect to the surrounding surface as well as to calculate the arithmetic surface average roughness (R_a) values for a large area of a given sample.

Electron backscatter diffraction

Electron backscatter diffraction (EBSD) methods were used to create orientational image mappings (OIM) of neighboring matrix grains in selected annealed CoCrMo samples. A Quanta ESEM with an EBSD detector was used to acquire and index diffraction patterns for multiple periodic 2D arrays of points on the sample surface. An accelerating
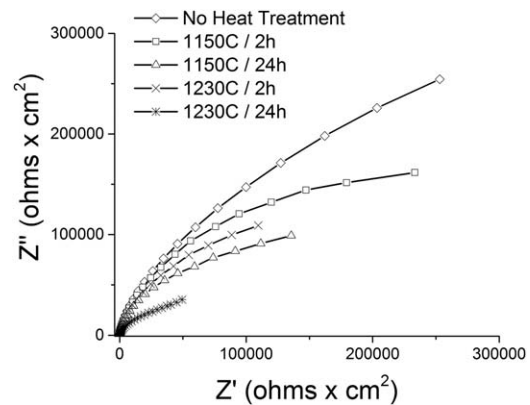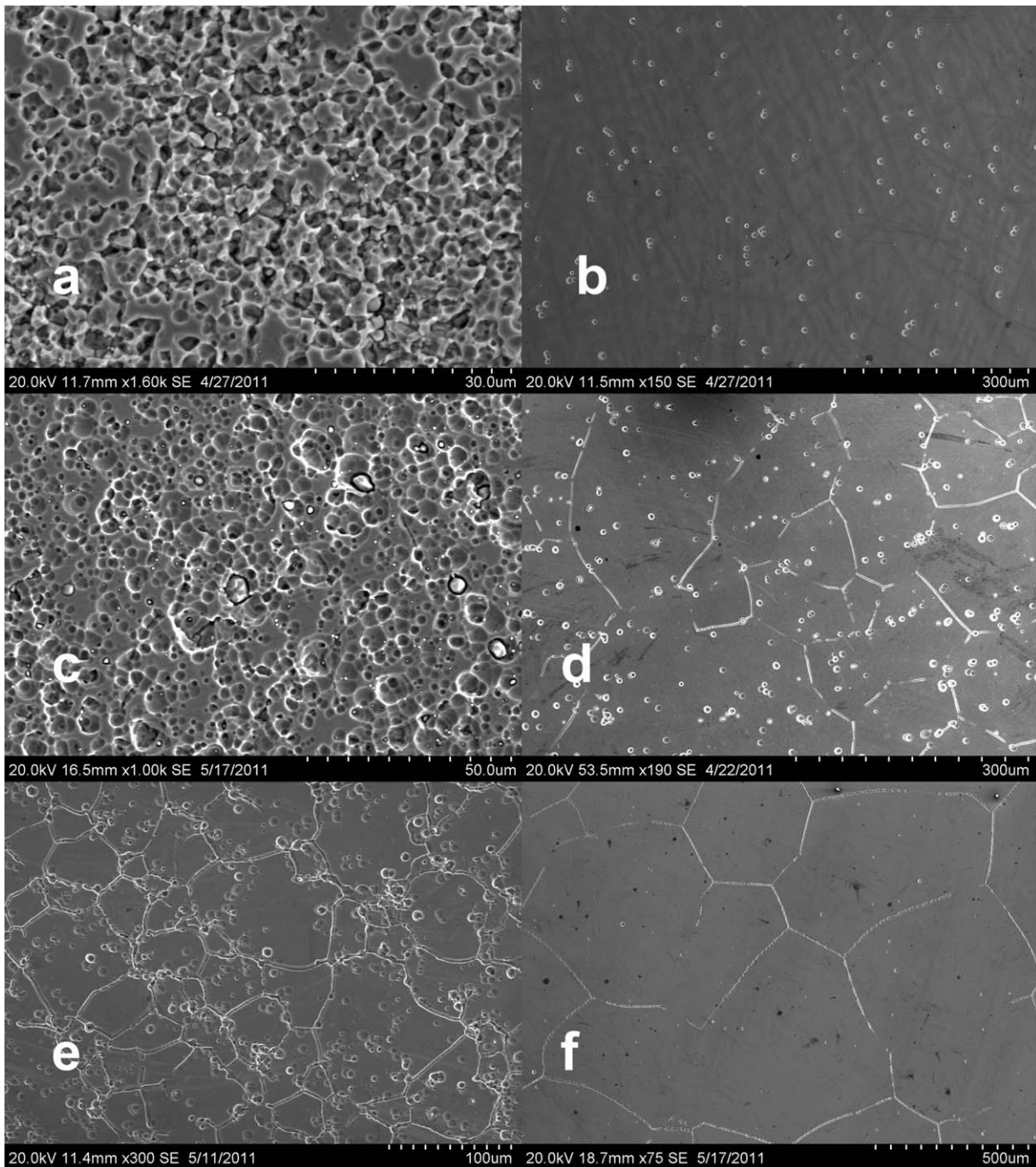

FIGURE 6. Experimental Nyquist plots of solution-annealed HC CoCrMo. A representative curve was chosen for each solution-annealed condition; impedance data was obtained in triplicate. Experimental Nyquist plots are in the form of depressed semicircles.

FIGURE 7. Corroded surface of (a) HC CoCrMo wrought alloy in absence of solution-annealing, (b) LC CoCrMo wrought alloy in absence of solution-annealing, (c) 1150°C, 2 h solution-annealed HC CoCrMo wrought alloy, (d) 1150°C, 24 h solution-annealed HC CoCrMo wrought alloy, (e) 1230°C, 2 h solution-annealed HC CoCrMo wrought alloy, and (f) 1230°C, 24 h solution-annealed HC CoCrMo wrought alloy.

voltage of 20 kV was chosen to maintain a suitable resolution and a sufficiently low level of noise. A step size of 0.4 μm was used, and the backscattered signal was collected for five frames of 0.1 s for each point in the array. Orientational indexing from the Kikuchi diffraction patterns was performed using the commercially available Oxford Flamenco EBSD processing software, assuming a single fcc-Co matrix phase.

Misorientation matrices for each grain boundary were calculated geometrically from Euler angles that mapped the orientation of the adjacent grains to the sample surface. Each grain boundary's three-dimensional misorientation was systematically identified as a high- or low-angle grain boundary. For the high-angle grain boundaries ($>15°$ misorientation angle), the Brandon Criterion[24] was used to determine the reciprocal coincident site lattice (CSL) density Σ

based on geometric three-dimensional misorientations with lattice coincidence for fcc crystals (Table IV), which correlates to the relative grain boundary energy. Fcc symmetry of each grain was taken into account from the 24 equivalent three-dimensional orientations in each fcc crystal.[25]

In this application of EBSD, the corroded samples were of poor surface quality (high roughness), resulting in blurred Kikuchi patterns and a lower fraction of indexed points on the array than a typical specimen prepared specially for EBSD. Due to a high area fraction of corrosion pits on all the HC CoCrMo samples without extensive annealing, only samples solution-annealed at 1230°C for 24 h were suitable for use with the EBSD technique in order to ensure greater than 90% of the points on the sampling array were successfully indexed. While the grain boundary character distribution is likely to vary between alloys with different heat treatments, correlations between grain boundary character and corrosion susceptibility/immunity are likely to translate across samples with different thermomechanical treatment.

Statistics

Orientational image maps were taken from four random areas of two corroded solution-annealed samples. The 102 grain boundaries sampled were used to determine the likelihood that a grain boundary of a certain misorientation would corrode under the experimental conditions used in this study. A two-sided 95% confidence interval was used to find the percent of cumulative grain boundary geometries within the total population that would be expected to corrode.

RESULTS

Heat treatment and processing

In agreement with prior work,[3,18,26] solution annealing the wrought CoCrMo alloys resulted in significant grain coarsening, seen in Figure 1a–d, quantitatively summarized in Figure 2. A larger degree of grain growth was observed for longer times (24 h) or at a higher temperature (1230°C). Partial second phase dissolution was observed in the HC wrought alloy as expected for this alloy,[17] and for solution-annealing biphasic alloys in general.[27] The high-carbon version of the alloy demonstrated slightly less grain growth from solution annealing than its low-carbon counterpart, most likely due to grain pinning by intermetallic and carbide phases.[27] While some of the solution-annealed alloys have a grain size larger than that allowed by the standard for use of this metal as a biomedical alloy, they are included in the corrosion analysis to further illustrate the relationship between grain size and corrosion behavior.

Electrochemistry

Table IV shows the electrochemical data, corrosion current (i_{corr}), corrosion potential (E_{corr}), and the free potential before and after polarization (E_{oc} before and E_{oc} after). The current density i_{corr}, extrapolated from the potentiodynamic curve [Figure 3] by means of Tafel's approximation,[21,22,28] diminished significantly from the wrought state to the
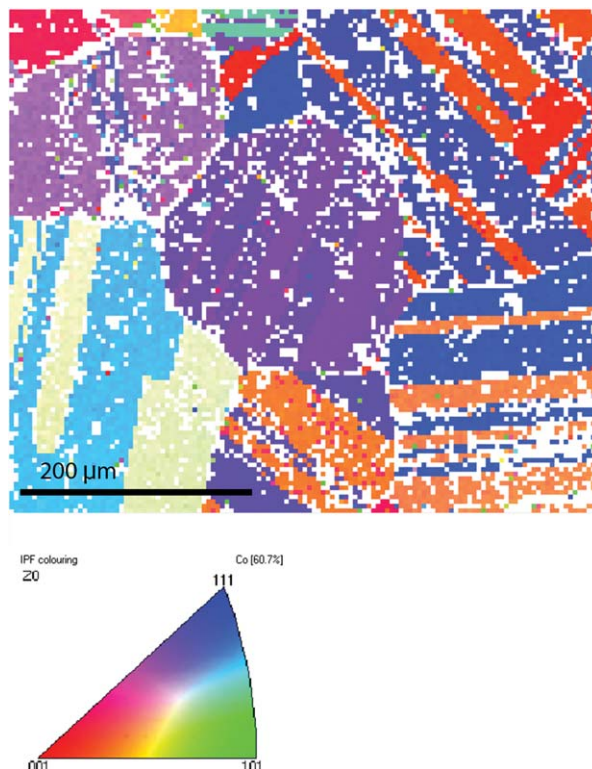

FIGURE 8. Orientational image mapping of corroded surface of 1230°C, 24 h solution-annealed HC CoCrMo wrought alloy. [Color figure can be viewed in the online issue, which is available at wileyonlinelibrary.com.]

solution-annealed state, as summarized in Figure 4. The lower i_{corr} values observed for the solution-annealed specimens are indicative of lower corrosion rates, thus signifying an improvement in the corrosion resistance. The potential range for passive behavior was approximately −0.25 V to 0.5 V vs. SCE across all HC CoCrMo samples, and the passive current was also found to be similar, as depicted in Figure 3. Anodic oxide breakdown potentials (transpassive potentials) were observed at around 0.5 V vs. SCE uniformly for all samples. All samples exhibited a secondary passivity around 0.7 V vs. SCE.

EIS data, including the polarization resistance (R_p) and capacitance, are included in Table IV. Representative Bode plots of the experimental data are depicted in Figure 5, and a Nyquist plot of representative experimental impedance data for each solution-anneal condition is depicted in Figure 6. All experimental impedance datasets were fit to the Randles (with CPE) circuit, with impedance given by

$$Z = R_s + \frac{1}{1/R_p + C(j\omega)^n}$$

where $0.7 < n < 1$ is the phase angle shift due to non-ideal behavior of the double layer capacitance. A complex non-linear least-squares (CNLS) analysis was performed to determine the best EC fit, and χ^2 values were consistently under 0.006. While lacking a strong statistical significance, there was a slight trend in polarization resistance wherein
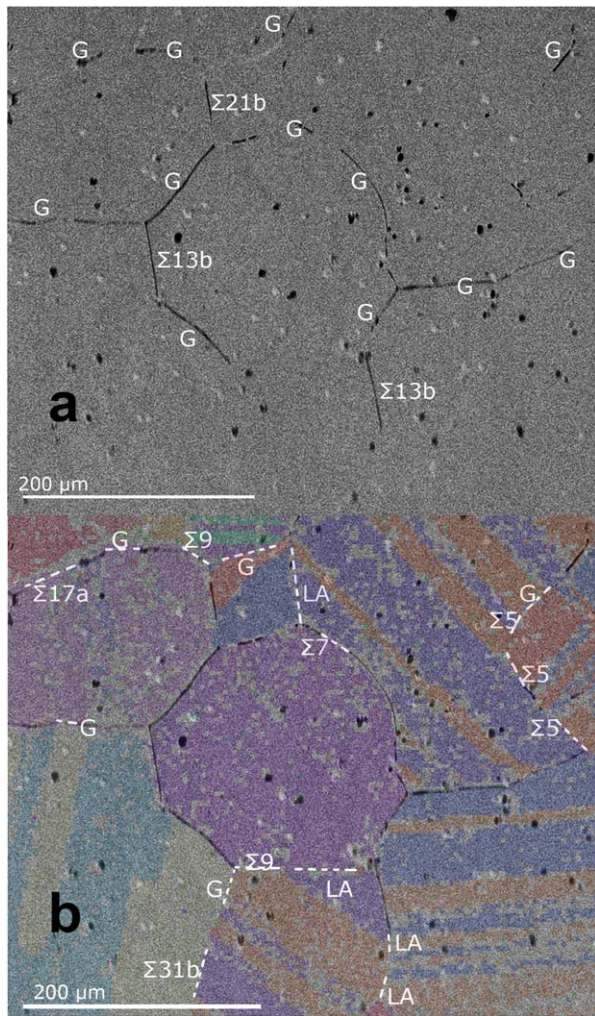
FIGURE 9. (a) Indexing of corroded grain boundaries based on OIM. (b) indexing of uncorroded grain boundaries based on OIM (overlayed). "G" indicates general grain boundary geometry with no lattice site coincidence, "LA" indicates low angle. [Color figure can be viewed in the online issue, which is available at wileyonlinelibrary.com.]

solution-annealed alloys had a lower R_p. This trend is not supported by that seen in i_{corr} values, but it should be noted that the potentiodynamic scan measures behavior at a range of potentials, while the impedance tests are conducted at only E_{corr}. This slight decrease in polarization resistance with solution annealing may be attributed to a variation in surface resistance due to second phase dissolution. This merits future study of EIS testing of CoCrMo at other potentials, particularly at a passivation potential (E_{pass}) and pitting potential (E_{pit}).

Corrosion morphology

SEM micrographs revealed the nature of electrochemical corrosion attacking the CoCrMo alloys. The corroded high-carbon alloys displayed pitting corrosion [Figure 7a, c–f], which occurs as a result of certain localized areas on the surface being more susceptible to corrosion. Corrosion pits were 1–3 µm in diameter and 2–6 µm in depth, as confirmed by interferometry. In passive alloys such as cobalt–

chromium, a corrosion pit initiates on the surface, removing a part of the protective passive film and allowing for more rapid autocatalytic corrosion to follow underneath in the absence of repassivation.[6] The corroded low-carbon alloys [Figure 7b] displayed very few corrosion pits at no discernable type of location but had uneven surface topography, as verified by white light interferometry, demonstrating that general surface corrosion was the primary mechanism applicable to alloys of low-carbon composition.

For the solution-annealed alloys with larger grain sizes, it was found that the pits in the HC alloy localized at phase boundaries [Figure 7c] and certain matrix grain boundaries [Figures 7d–f]. This behavior has been observed previously in 316L stainless steel implant retrievals, which also rely on a chromium oxide layer as a barrier to corrosion.[6] The absence of grain boundary corrosion in the low-carbon CoCrMo may be a sign that chromium is not depleted and there is no segregation at the grain boundaries, since chromium-rich carbides do not form while processing this version of the alloy. In unannealed HC samples, corrosion pits were observed at a dramatically higher number density per surface area, primarily due to the smaller grain size and presence of more boundaries in a given unit of surface area.

The concept of coincident site lattice (CSL) is useful in the classification of grain boundaries in this case, because it allows for prediction of local properties, including corrosion resistance, based on the geometrical misorientation between

TABLE V. Coincident Site Lattice Misorientations for fcc Crystals

Σ	Rotation Angle, °	Rotation Axis		
		u	v	w
3	60	1	1	1
5	36.86	1	0	0
7	38.21	1	1	1
9	38.94	1	1	0
11	50.47	1	1	0
13a	22.62	1	0	0
13b	27.79	1	1	1
15	48.19	2	1	0
17a	28.07	1	0	0
17b	61.9	2	2	1
19a	26.53	1	1	0
19b	46.8	1	1	1
21a	21.78	1	1	1
21b	44.41	2	1	1
23	40.45	3	1	1
25a	16.26	1	0	0
25b	51.68	3	3	1
27a	31.59	1	1	0
27b	35.43	2	1	1
29a	43.6	1	0	0
29b	46.4	2	2	1
31a	17.9	1	1	1
31b	52.2	2	1	1
33a	20.1	1	1	0
33b	33.6	3	1	1
33c	59.0	1	1	0
35a	34.0	2	1	1
35b	43.2	3	3	1
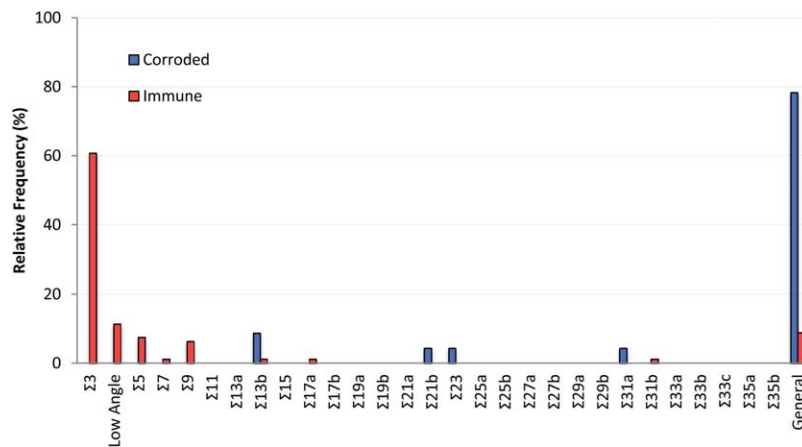
FIGURE 10. Relative frequencies of grain boundary geometries for corroded and immune boundaries. Fcc grain boundary geometries listed in order of decreasing lattice coincidence and increasing energy. [Color figure can be viewed in the online issue, which is available at wileyonlinelibrary.com.]

grains. The special CSL grain boundaries are characterized by the parameter Σ, which is the ratio of coincident lattice sites and crystal unit cell volumes. Previous work on stainless steel, copper, nickel, and aluminum alloys demonstrated that, in accordance with CSL theory, grain boundaries with a low reciprocal coincident lattice density (Σ) had a relatively low energy compared to "general" or high Σ boundaries.[29–33] The studies on microtexture of stainless steels showed that low-Σ grain boundaries exhibited less chromium depletion.[29,30]

The results of EBSD orientational imaging are shown in Figure 8. Over 85% of points in the OIM array were successfully indexed for multiple locations on the corroded sample, and only grains with over 20 indexed points were included for average grain orientation analysis. The misorientation axes and angles for several (102) corroded [Figure 9a] and "immune" [Figure 9b] grain boundaries were compared to those of low-Σ ($\Sigma 3 - \Sigma 35$) coincident site lattice geometries for fcc crystals shown in Table V using the tolerance as defined by the Brandon Criterion,[24,25] $\Delta\theta \leq 15°(\Sigma^{-1/2})$. The Brandon Criterion is widely accepted and used in this study to determine when experimentally determined grain boundary misorientations are sufficiently close to the special CSL geometries to exhibit the improved grain boundary properties. The results of this grain boundary characterization are summarized in Figure 10. Of the grain boundary geometries with at least two observations, 100% of all reciprocal coincident lattice site densities of 9 or lower (and low-angle grain boundaries) did not corrode while only 30.4% of general high-angle grain boundaries did not corrode [Figure 11]. Based on the 102 grain boundaries observed, we can be 95% confident that over 90% of the grain boundaries with reciprocal lattice coincidence $\Sigma 21b$ or lower will be immune to the *in vitro* electrochemical corrosion applied in this study, as shown in Figure 12. In general, the grain boundaries that were immune to corrosion were low-energy, either low-angle or high in degree of coincidence. Grain boundaries that were susceptible to corrosion were high-energy, having both a high-angle and low

degree of lattice coincidence. This energy-dependent grain boundary corrosion behavior was similar to that observed by Palumbo & Aust in nickel alloys and stainless steels.[32,34]

DISCUSSION

Both electrochemical data and SEM micrographs of the corrosion morphology demonstrate that the rate of corrosion and surface density of corrosion pits decrease when a high-carbon CoCrMo alloy is annealed from the wrought state to increase grain size and partially dissolve second phases. While current ASTM standards for the application of hip implant materials do not place restrictions on the minimum grain size and do not recommend specific processing schemes for reduced corrosion,[16] this evidence suggests that slight variations in the thermomechanical processing and resultant microstructure have a direct and significant effect on corrosion, one of the main degradation processes affecting these medical devices. Prior implant retrieval studies have pointed to intergranular corrosion as a mechanism for degradation in cobalt-based alloys, but have not yet discerned any trends on which grain boundaries (if any) are less susceptible to corrosion.[35,36]

Even though finer grains are traditionally preferred to improve the mechanical properties and increase wear
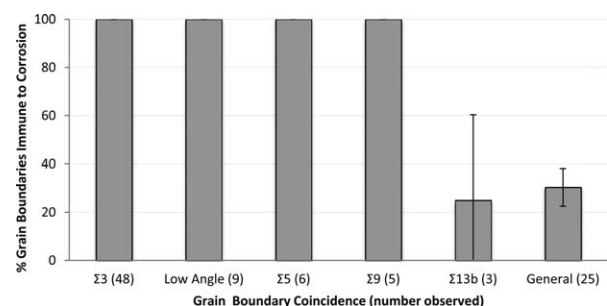
FIGURE 11. Percent of grain boundaries of various geometries that were immune to corrosion. Grain boundary geometries with fewer than two observations were omitted from statistical analysis.
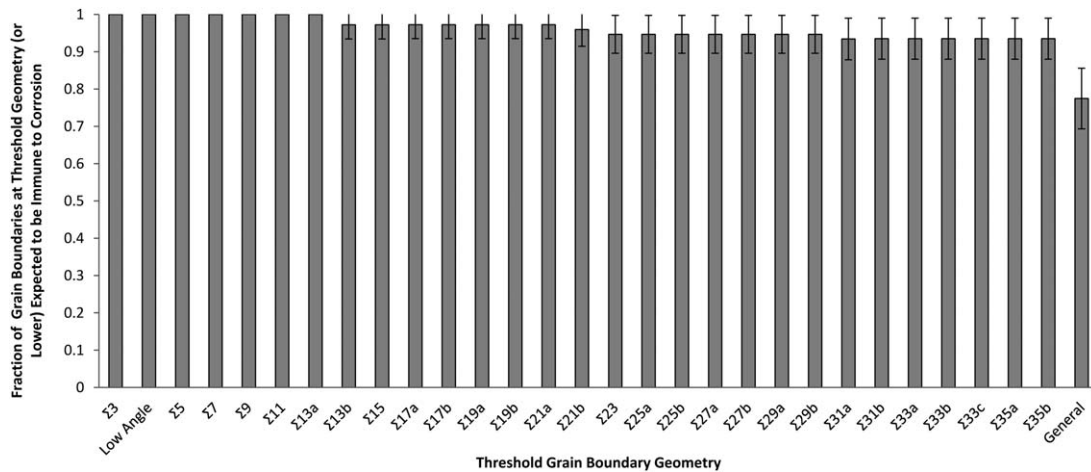
FIGURE 12. Fraction of grain boundaries at or below various threshold geometries that are expected to be immune to corrosion. Using a 95% confidence interval, over 90% of grain boundaries with reciprocal lattice coincidence Σ21b or lower can be expected to be immune to the *in vitro* electrochemical corrosion applied in this study. A total of 69–86% of all grain boundaries (both general and those of special CSL geometries) will be immune.

resistance,[6,37,38] coarser grains may be advantageous in improving the alloy's corrosion resistance. The implications of this study are that for the metal at the articulating interface of hip implants, there may exist an optimum grain size to effectively minimize the combined damage from wear and corrosion. However, this remains an open question since the two degradation processes do not behave independently, with each accelerating the other, and the implant is also affected by grain refinement for the first few hundreds of nanometers from the articulating surface.[39,40] An alternative to grain coarsening may be to develop a processing scheme via grain boundary engineering to have fine grains but to promote a higher % of low-angle or high coincidence grain boundaries. Through grain boundary engineering, the fraction of low-Σ boundaries, typically between 30% and 60% in conventionally processed materials, can be increased up to 80%. During the annealing processes of grain boundary engineering, low-energy, lower-mobility boundaries increase in length as higher-mobility boundaries are consumed as a consequence of grain growth.[41] For CoCrMo in non-articulating surfaces such as the femoral neck and stem, a grain size on the coarser end of the allowable range ($\sim$50 μm)[16] may be ideal since these implant–tissue interfaces are subject to corrosion but not mechanical wear.

Whether grain boundary corrosion is beneficial or detrimental to the implant's longevity in general is an open question. While heat processing the alloy to eliminate the phase boundaries and grain boundaries might seem unconditionally helpful in promoting corrosion resistance, it is possible that some grain boundaries act as a sacrificial anode in a micro-galvanic system and protect the rest of the implant surface.[28]

CONCLUSIONS

The mechanism for corrosion is different between low-carbon and high-carbon versions of the CoCrMo implant alloy, with the former undergoing general corrosion when an anodic potential is applied and the latter being susceptible to intergranular pitting corrosion. This suggests that elemental segregation may be partially responsible for the localized pitting corrosion behavior in HC CoCrMo. The effects from solution annealing, namely grain coarsening and partial dissolution of second phases, reduce the rate of corrosion for wrought HC CoCrMo alloys. This is attributed to the decrease in vol% of the phase boundary and grain boundary areas during this process. The effects from solution annealing do not improve or diminish the corrosion properties of the Cr_2O_3 passive film. Grain boundary energy is partially responsible for determining which grain boundaries are susceptible and which are immune to corrosion. Lower-energy grain boundaries (i.e., low-angle or high-angle and high degree of lattice coincidence) were found to be more resistant to corrosion.

REFERENCES
1. Kurtz S, Ong K, Lau E, Mowat F, Halpern M. Projections of primary and revision hip and knee arthroplasty in the United States from 2005 to 2030. J Bone Joint Surg 2007;89:780–785.
2. Pramanik S, Agarwal AK, Rai KN. Chronology of total hip joint replacement and materials development. Trends Biomat Artif Organs 2005;19:15–26.
3. Clemow AJT, Daniell BL. Solution treatment behavior of Co–Cr–Mo alloy. J Biomed Mater Res 1979;13:265–279.
4. Gomez M, Mancha H, Salinas A, Rodrigues J, Escobedo J, Castro MR, Mendez M. Relationship between microstructure and ductility of investment cast ASTM F-75 implant alloys. J Biomed Mater Res 1997;34:157–163.
5. Nevelos J, Shelton J, Fisher J. Metallurgical considerations in the wear of metal-on-metal hip bearings. Hip Int 2004;14:1–10.
6. Ratner BD, Hoffman AS, Schoen FJ, Lemons JE, editors. Biomaterials Science: An Introduction to Materials in Medicine, 2nd ed. Elsevier; 2004.

7. Saldivar-Garcia A, Lopez H. Microstructural effects on the wear resistance of wrought and as-cast Co–Cr–Mo–C implant alloys. J Biomed Mater Res A 2005;74A:269–274.

8. Hallab N, Merritt K, Jacobs JJ. Metal sensitivity in patients with orthopaedic implants. J Bone Joint Surg 2001;83:428436.

9. Gilbert J, Buckley C, Jacobs JJ. In-vivo corrosion of modular hip-prosthesis components in mixed and similar metal combinations – the effect of crevice, #stress, lmotion, and alloy coupling. J Biomed Mater Res 1993;27:1533–1544.

10. Gilbert J, Mali S, Urban RM, Silverton C, Jacobs JJ. In vivo oxide-induced stress corrosion cracking of Ti–6Al–4V in a neck-stem modular taper: Emergent behavior in a new mechanism of in vivo corrosion. J Biomed Mater Res B 2012;100B: 584–594.

11. Yan Y, Neville A, Dowson D, Williams S. Tribocorrosion in implants – assessing high carbon and low carbon Co–Cr–Mo alloys by in situ electrochemical measurements. Tribol Int 2006; 39:1509–1517.

12. Amstutz HC, Campbell PA, Dorey FJ, Johnson AJ, Skipor AK, Jacobs JJ. Do ion concentrations after metal-on-metal hip resurfacing increase over time?. A prospective study. J Arthroplasty 2013;28:695–700.

13. Merritt K, Brown SA. Distribution of cobalt chromium wear and corrosion products and biologic reactions. Clin Orthop Relat R 1996;329:S233–S243.

14. Vendittoli PA, Mottard S, Roy AG, Dupont C, Lavigne M. Chromium and cobalt ion release following the Durom high carbon content, forged metal-on-metal surface replacement of the hip. J Bone Joint Surg Br 2007;89:441–448.

15. Witzleb WC, Zeigler J, Krummenauer F, Neumeister V, Guenther KP. Exposure to chromium, cobalt and molybdenum from metal-on-metal total hip replacement and hip resurfacing arthroplasty. Acta Orthop 2006;77:697–705.

16. Standard specification for wrought cobalt-28–chromium-6–molybdenum alloys for surgical implants (UNS R31537, UNS R31538, and UNS R31539). Volume designation F 1537-08. West Conshohocken, PA: ASTM International; 2008.

17. Caudillo M, Herrera-Trejo M, Castro MR, Ramirez E, Gonzalez CR, Juarez Jl. On carbide dissolution in an as-cast ASTM F-75 alloy. J Biomed Mater Res 2002;59:378–385.

18. Gupta KP. The Co–Cr–Mo (cobalt–chromium-molybdenum) system. J Phase Equilib Diff 2005;26:87–92.

19. Kilner T, Pilliar RM, Weatherly GC, Allibert C. Phase identification and incipient melting in a cast Co–Cr surgical implant alloy. J Biomed Mater Res 1982;16:63–79.

20. Vidal CV, Munoz AI. Study of the adsorption process of bovine serum albumin on passivated surfaces of CoCrMo biomedical alloy. Electrochim Acta 2010;55:8445–8452.

21. Tafel J. Uber die Polarisation bei kathodischer Wasserstoffentwicklung. Z Phys Chem-Stock Ve 1905;50:641–712.

22. Tafel J, Naumann K. Beziehungen zwischen Kathodenpotential und elektrolytischer Reduktionswirkung. Z Phys Chem-Stock Ve 1905;50:713–752.

23. Blunt RT. White light interferometry – a production worthy technique for measuring surface roughness on semiconductor wafers. 2006 April 24–27; Vancouver, British Columbia, Canada. p 59–62.

24. Brandon DG. The structure of high-angle grain boundaries. Acta Metall 1966;14:1479–1484.

25. Randle V, Engler O. Introduction to Texture Analysis: Macrotexture, Microtexture and Orientation Mapping. CRC Press; 2000.

26. Rajan K. Thermodynamic assessment of heat treatments for a Co–Cr–Mo alloy. J Mater Sci 1983;18:257–264.

27. Doherty RD, Hughes DA, Humphreys FJ, Jonas JJ, Jensen DJ, Kassner ME, King WE, McNelley TR, McQueen HJ, Rolletti AD. Current issues in recrystallization: a review. Mat Sci Eng A – Struct 1997;238:219–274.

28. Talbot D, Talbot J. Corrosion Science and Technology. Boca Raton, FL: CRC Press LLC; 1998.

29. Bennett BW, Pickering HW. Effect of grain boundary structure on sensitization and corrosion of stainless steel. Metall Trans A 1987; 18A:1117–1124.

30. Kurban M, Erb U, Aust KT. A Grain boundary characterization study of boron segregation and carbide precipitation in alloy 304 austenitic stainless steel. Scripta Mater 2006;54:1053–1058.

31. Miyamoto H, Ikeuchi K, Mimaki T. The role of grain boundary plane orientation on intergranular corrosion of symmetric and asymmetric [1 1 0] tilt grain boundaries in directionally solidified pure copper. Scripta Mater 2004;50:1417–1421.

32. Palumbo G, Aust KT. Structure-dependence of intergranular corrosion in high purity nickel. Acta Metall Mater 1990;38:2343–2352.

33. Yuan Y, Ambat R, Strangwood M, Davenport AJ, Afseth A, Scamans G. Crystallographic effects in intergranular corrosion of an Al–Mg alloy. In: Sinclair J, Frankenthal R, Kalman E, Plieth W, editors. Corrosion and Corrosion Protection. Pennington, NJ: The Electrochemical Proceeding Series; 2001. p 273.

34. Palumbo G, Aust KT. Solute effects in grain boundary engineering. Can Metall Quart 1995;34:165–173.

35. Gilbert J, Buckley C, Jacobs JJ, Bertin K, Zernich M. Intergranular corrosion-fatigue failure of cobalt-alloy femoral stems. A failure analysis of two implants. J Bone Joint Surg Am 1994;76:110–115.

36. Kop A, Swarts E. Corrosion of a hip stem with a modular neck taper junction: A retrieval study of 16 cases. J Arthroplasty 2009; 24:1019–1023.

37. Devine TM, Wulff J. Cast vs. wrought cobalt–chromium surgical implant alloys. J Biomed Mater Res 1975;9:151–167.

38. Sato Y, Nomura N, Fukinuma S, Chiba A. Microstructure and mechanical properties of hot-pressed Co–Cr–Mo alloy compacts. Adv Mat Res 2007;26–28:769–772.

39. Buscher R, Fischer A. The pathways of dynamic recrystallization in all-metal hip joints. Wear 2005;259:887–897.

40. Pourzal R, Theissmann R, Williams S, Gleising B, Fisher J, Fischer A. Subsurface changes of a MoM hip implant under different contact zones. J Mech Behav Biomed Mater 2009;2:186–191.

41. Schlegel S, Hopkins S, Frary M. Effect of grain boundary engineering on microstructural stability during annealing. Scripta Mater 2009;61:88–91.